Available online at www.sciencedirect.com
ScienceDirect
Icarus 195 (2008) 698–704
ICARUS
www.elsevier.com/locate/icarus

The topographic limits of gravitationally bound, rotating sand piles

David A. Minton *

Lunar and Planetary Laboratory, The University of Arizona, Tucson, AZ 85721, USA

Received 31 July 2007; revised 28 November 2007

Available online 8 March 2008

Abstract

Rubble pile asteroids can attain shapes that are dramatically different from those of rotating, self-gravitating equilibrium fluids. A new numerical technique, called "seed growth," is demonstrated for calculating three-dimensional bodies that are self-gravitating and rotating, and whose every surface is approximately at a constant angle, ϕ, with respect to the local horizontal. By altering the configuration of cusps, which are points along a constant longitude path where the surface angle changes sign but not magnitude, multiple solution shapes that satisfy the condition that all surface slopes are at a constant angle are possible. Five different cusp configurations are explored here, three of which yield solutions for $20^\circ \leqslant \phi \leqslant 30^\circ$. Rotational effects are explored, and it is found that for some solution shapes, the ratios of their shortest to longest dimensions, c/a, can fall outside the limits published in the literature for rotating, cohesionless, spheroidal bodies. Solution shapes show some similarities to observed small bodies, such as the saturnian satellite Atlas, the near-Earth Asteroid 1999 KW4, and some contact binary asteroids.

Keywords: Asteroids; Asteroids, surfaces; Satellites, shapes

1. Introduction

Many asteroids are likely to be aggregations of collisional fragments, so-called "gravitational aggregates" (Richardson et al., 2002). Gravitational aggregates are often called "strengthless," however internal friction and interlocking between particles can maintain topography that is out of hydrostatic equilibrium. One can observe that loose piles of aggregated particles, like sand, have slopes that are maintained at what is called the *angle of repose*, ϕ, where typically $20^\circ \lesssim \phi \lesssim 30^\circ$ with respect to horizontal (Bretz et al., 1992; Buchholtz and Pöschel, 1994). The purpose of this study is to explore the topographic limits of a hypothetical asteroid composed entirely of loose sand. What would a self-gravitating, rotating sand pile look like if every slope on the surface was at the angle of repose?

Other attempts have been made to establish the shapes of angle of repose-limited rubble pile asteroids using a variety of techniques. Withers (2000) attempted to calculate axisymmetric shapes by randomly varying surface profiles of homogeneous shapes until the calculated mean slope angle was near 30°, with mixed success. Holsapple (2001, 2004, 2007) and Holsapple and Michel (2006) derived generalized limits of cohesionless solid spheroidal and ellipsoidal elastic–plastic bodies using a Mohr–Coloumb yield criterion for the limiting internal stress state, including the effects of rotation and tidal forces. Richardson et al. (2005a) used numerical simulations of aggregates of smooth, rigid, spherical particles and produced quasi-ellipsoidal aggregates whose dimensions were consistent with limits derived by Holsapple (2001) for $\phi = 40^\circ$.

The approach of this paper is to consider the geometrical problem of calculating uniform density, three-dimensional objects for which the surface at every point is at an angle ϕ relative to the local horizontal as defined by the sum of the gravitational and centripetal acceleration vectors at that point. To solve this geometrical problem I have developed an iterative numerical technique called the "seed growth" technique.

2. The seed growth technique

Consider a body with some arbitrary cross section defined by the surface $\rho = f(\psi, \theta)$, where ρ is the radial distance from the body's center of mass, ψ is the longitude, and θ is the co-

* Fax: +1 (520) 621 4933.
E-mail address: daminton@lpl.arizona.edu.

0019-1035/$ – see front matter
doi:10.1016/j.icarus.2008.02.009

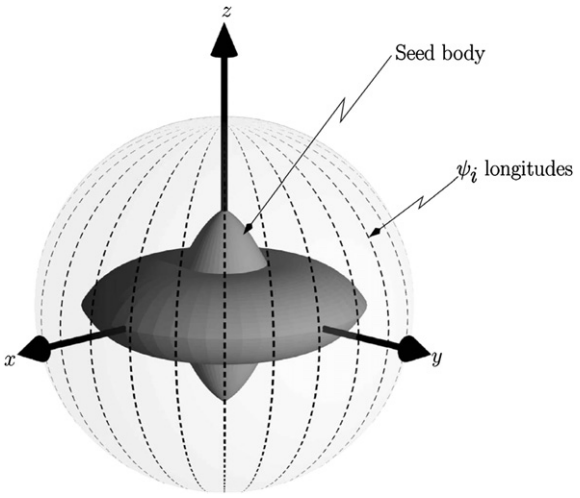

Fig. 1. An illustration of the coordinate system used in this work. The gravitational acceleration vector, **g**, is calculated along each profile using the seed body. Each profile follows a single longitude, ψ_i. For non-rotating bodies, and for bodies with rotation about the z-axis only, the z-axis is a symmetry axis.

latitude. The problem is to identify the solid bounded by the surface $\rho = f(\psi, \theta)$ that is always at an angle, ϕ, relative to the local gravitational horizontal. This can be expressed by the following equation:

$$\hat{\mathbf{N}} \cdot \hat{\mathbf{g}}_{\text{eff}} + \cos\phi = 0, \tag{1}$$

where $\hat{\mathbf{N}}$ is the unit normal vector at a point on the surface, and $\hat{\mathbf{g}}_{\text{eff}}$ is the effective gravitational unit vector at the same point, which includes contributions from the gravitational and the centripetal acceleration vectors. If $\phi = 0$, then Eq. (1) describes a fluid in hydrostatic equilibrium, and analytical solutions for isolated bodies were found by Maclaurin and Jacobi (e.g., Chandrasekhar, 1969). For the case where $\phi \neq 0$ everywhere, no closed-form analytical solutions are known.

Three-dimensional shapes that are approximate solution to Eq. (1) can be found using some simplifying assumptions and an iterative technique I call "seed growth." The first simplifying assumption I make is to approximate the three-dimensional body as a finite set of two-dimensional profiles, with each profile confined to a plane containing all lines of constant longitude ψ_i. Note that when constructing solutions the terms "latitude," "longitude," and "pole" of the body are used without regard to the body's rotation axis, which can be chosen arbitrarily. An illustration of the coordinate system used here is shown in Fig. 1. A consequence of this simplifying assumption is that, for non-rotating solution shapes and for solution shapes rotating about the z-axis, the solution bodies are axisymmetric about the z-axis.

Because I am calculating two-dimensional profiles that are confined to a single plane, the unit tangent vector of the profile is used instead of the unit surface normal vector of the body, thereby simplifying the calculation. Instead of using Eq. (1), the profile slope is constrained with the equation:

$$\hat{\mathbf{T}} \cdot \hat{\mathbf{g}}_{\text{eff}} + \sin\phi = 0. \tag{2}$$

Equation (2) is not, in general, equivalent to Eq. (1) because there is no guarantee that a constant longitude path is the "most uphill" or "most downhill" path on a body. However, in this work all solution shapes whose longitudinal profiles satisfy Eq. (2) were found to also satisfy Eq. (1). The position vector along a two-dimensional ψ_i profile can be written as the following vector-valued function:

$$\mathbf{S}_i = \rho(\theta, \psi_i) \cdot \left[\cos\psi_i \sin\theta \cdot \hat{\mathbf{x}} + \sin\psi_i \sin\theta \cdot \hat{\mathbf{y}} + \cos\theta \cdot \hat{\mathbf{z}}\right]. \tag{3}$$

The tangent vector along a two-dimensional profile is therefore:

$$\begin{aligned}\mathbf{T}_i = {} & \cos\psi_i \left(\rho\cos\theta + \frac{\mathrm{d}\rho}{\mathrm{d}\theta}\sin\theta\right)\hat{\mathbf{x}} \\ & + \sin\psi_i \left(\rho\cos\theta + \frac{\mathrm{d}\rho}{\mathrm{d}\theta}\sin\theta\right)\hat{\mathbf{y}} \\ & - \left(\rho\sin\theta - \frac{\mathrm{d}\rho}{\mathrm{d}\theta}\cos\theta\right)\hat{\mathbf{z}}.\end{aligned} \tag{4}$$

Beginning with some initial radial distance ρ_0, a profile along the ith longitude is generated by substituting Eq. (4) into Eq. (2), solving for $\mathrm{d}\rho/\mathrm{d}\theta$, and then numerically integrating from $\theta_1 = 0$ in $\Delta\theta$ increments to $\theta_m = \pi$. In order to perform this integration, the effective gravitational unit vector along the profile must also be known.

The effective gravitational unit vector depends on the shape of the body, so it cannot be calculated a priori. The seed growth technique overcomes this limitation by utilizing "seed" bodies to "grow" solutions iteratively. Iteration begins with an initial seed shape. The initial seed shape is generated using a simplified model of the object's gravitational field where only the $1/r$ and rotational components of the potential are considered, neither of which depends on the shape of the body. Starting at longitude $\psi_1 = 0$ and marching in $\Delta\psi$ increments to $\psi_n = 2\pi - \Delta\psi$, new profiles are computed using the shape of the seed body to calculate the local acceleration unit vector, $\hat{\mathbf{g}}_{\text{eff}}$.

Once all n longitudinal profiles have been calculated, they are combined to produce an approximate three-dimensional solution shape. The solution shape is made of $2nm - 6$ triangular facets, with facet vertices at either $(\rho_{i,j}, \rho_{i+1,j}, \rho_{i+1,j+1})$ or $(\rho_{i,j}, \rho_{i,j+1}, \rho_{i+1,j+1})$, where $\rho_{i,j} = \rho(\theta_j, \psi_i)$. The solution shape after one iteration becomes the seed body for the next, and iteration continues until either convergence to a shape with a constant ϕ surface is achieved or the profile generation fails in some way. A solution shape is considered converged when the surface angle of all facets lies within $\pm 1^\circ$ of the target angle, ϕ. Profile generation fails either when a singularity develops in the seed body or the centripetal acceleration becomes greater than the gravitational acceleration at some point along the profile.

The term "angle of repose" refers to the magnitude of the slope, but the sign of the slope along a profile can abruptly change at "cusps." Cusps can be either point or line cusps and can be have a "positive" or a "negative" orientation, where a positive cusp is analogous to the sharp peak of a mound of loose material whose sides are at the angle of repose, and a negative

Table 1
Classification of cusp configurations based on number and sign of point and line cusps

Configuration name	Point cusps		Line cusps		Cusp latitudinal spacing
	+	−	+	−	
Heart	1	1	0	0	180°
Donut	0	2	1	0	90°
Dumbbell	2	0	0	1	90°
Hourglass	0	2	2	1	45°
Top	2	0	1	2	45°

For these configurations, cusps are spaced in equal increments of latitude along a profile. The corresponding seed profiles generated by these cusp configurations is shown in Fig. 2.

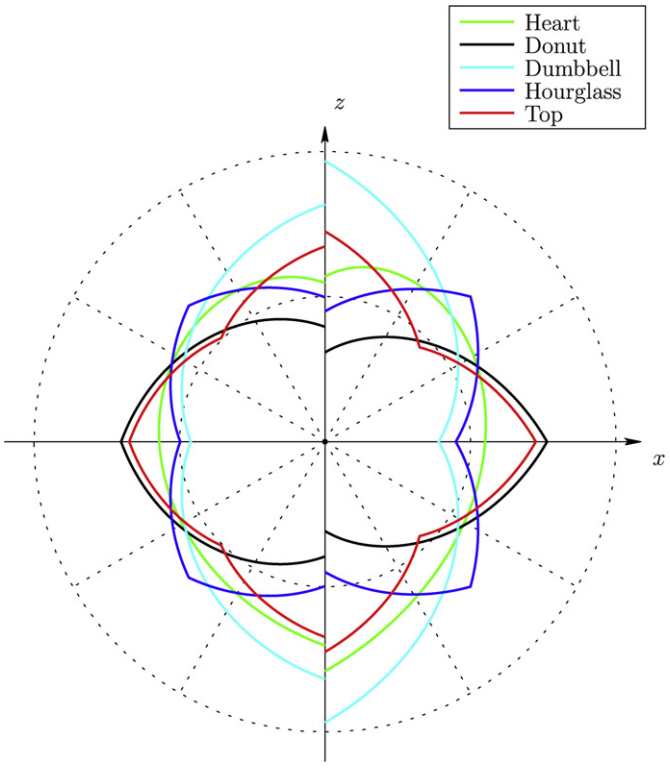

Fig. 2. Initial non-rotating seed profiles for the five different cusp configurations that were investigated. The profiles on the left are for $\phi = 20°$, and the profiles on the right are for $\phi = 30°$. Density was chosen to be $\sigma = 1500\ \mathrm{kg\,m^{-3}}$ and mass was 10^{13} kg. Circles mark intervals of 1000 m.

cusp is analogous to the bottom of a pit whose walls are at the angle of repose. In the coordinate system used here, illustrated in Fig. 1, a cusp that occurs at one of the poles is a point cusp, and one that occurs at some other latitude is a line cusp. The number and placement of cusps is a free parameter, though not all configurations result in solution shapes. When $\phi > 0$ everywhere, there must be at least two point cusps (one at each pole), but there can be any number of line cusps. There is no limit to either the number or configuration of line cusps, therefore there may be no unique solution to Eq. (1) for any given value of ϕ and rotation rate.

The gravitational vector, $\mathbf{g}$, along successive profiles is calculated numerically using the Fortran code *Polygrav* (see Richardson et al., 2005b), which rapidly calculates the gravitational acceleration vector due to the discretized seed shape. Following Werner (1994), *Polygrav* uses the Gauss Divergence Theorem to convert the calculation of the gravitational potential from a volume integral to a surface integral, assuming that the body has a uniform density. The effective gravitational vector is simply $\mathbf{g}_{\mathrm{eff}} = \mathbf{g} + \mathbf{a}_c$, where $\mathbf{a}_c$ is the centripetal acceleration vector.

The *Polygrav* code was combined with an implementation of the seed growth technique into a code called *Sandyroid* that generates approximate solutions to Eq. (1) subject to the constraints mentioned above. *Sandyroid* also takes advantage of any symmetries in seed shapes. For an axisymmetric configuration, only a single profile is calculated, which is then cloned for all n longitudes. Also, if the x–y plane is a symmetry plane, profiles are only calculated from $\theta = 0$ to $\theta = \pi/2$ and are then mirrored. At the end of each iteration, *Sandyroid* also scales the body to conserve its volume, and, because constant density is assumed, this automatically conserves its mass. If necessary, *Sandyroid* also shifts the center of the coordinate system to coincide with the center of mass.

2.1. Non-rotating solutions

Because the number and configuration of cusps is unconstrained, only a small subset of possible solutions were explored. The search for solution shapes was limited to angles of repose in the range of $20° \leqslant \phi \leqslant 30°$ and to five different cusp configurations. Cusp configurations are classified on the basis of type, number, location, and orientation (sign) of cusps. Table 1 lists the five configurations that were explored for this work, and Fig. 2 illustrates initial non-rotating seed profiles for these configurations.

The simplest configuration is "Heart," which contains point cusps at both poles. No solutions to Eq. (1) were found for the "Heart" configuration for $\phi \geqslant 20°$. Adding a line cusp at $\theta = 90°$ produced the two configurations "Dumbbell" and "Donut." No solutions were found for Dumbbell, but solutions were found for Donut with $\phi \lesssim 21°$. The two final configurations that were explored were "Top" and "Hourglass," which have line cusps at $\theta = 45°$, 90°, and 135° in addition to the polar point cusps. Solutions were found for Top with $\phi \lesssim 22°$ and for Hourglass with $\phi \lesssim 28°$. Fig. 3 shows the final profiles of these configurations for their highest-angle solutions, and Fig. 4 shows three-dimensional views of the same solutions.

Fig. 4 demonstrates that the surface angles of the final solution meshes are within approximately ±1° of the target surface angles. The deviations are primarily due to the discretization of the solution shapes into meshes of flat triangular facets, and higher resolution meshes show smaller deviations. Because the calculation of each point along a profile during an iteration requires a summation over all facets of the seed mesh, computation time can quickly become prohibitively expensive as the resolution is increased.

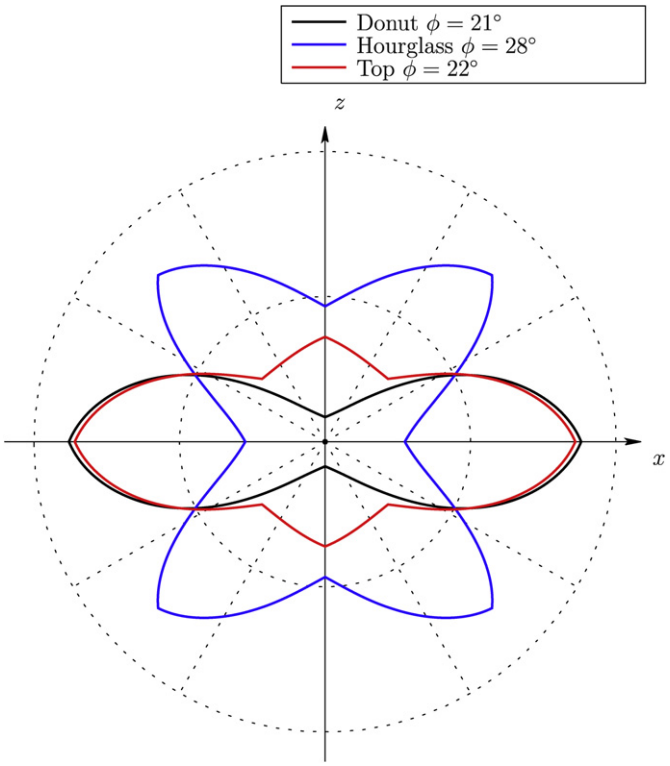

Fig. 3. Highest-angle, non-rotating constant surface angle solution profiles for the three configurations for which solutions were found. Density was chosen to be $\sigma = 1500\ \mathrm{kg\,m^{-3}}$ and mass was 10^{13} kg. Circles mark intervals of 1000 m. For these non-rotating solutions, the bodies are axisymmetric about the z-axis.

2.2. *Rotating solutions*

Sandyroid is able to calculate solution shapes with rotation about the x-, y-, or z-axes. If a solution is found, then the principal moments of inertia of the solution shape are calculated to determine whether or not the chosen axis is a stable rotation axis (the axis of maximum moment of inertia). Because of the way *Sandyroid* constructs seeds, and the symmetries of the cusp configurations chosen for this study, the x-, y-, and z-axes are also principal axes. Only solutions that have rotation about a stable axis are considered here.

The first rotational case considered for which solutions were found is the "Oblate Donut," which has the same cusp configuration as Donut, but with rotation about the z-axis. By varying the rotation rate as well as the angle of repose, a direct comparison can be made with Holsapple (2001), who explored equilibrium configurations of rubble piles using an internal yield stress criterion, rather than the purely geometrical criterion chosen for this study. For comparison with Holsapple's work, a similar notation system is adopted, and the two ratios of object dimensions are given as:

$$\alpha = c/a,$$
$$\beta = b/a, \tag{5}$$

where the dimensions are defined to be the maximum extent of the object along a principal axis, and $a \geqslant b \geqslant c$.

The results of several Oblate Donut solution shapes determined by *Sandyroid* are compared to the equilibrium configurations determined by Holsapple (2001) for oblate spheroids in Fig. 5. Note that *Sandyroid* is capable of reproducing a portion of the classic Maclaurin spheroid curve when given $\phi = 0°$. For $\phi > 0°$ *Sandyroid* produces a lower value of α for any given rotation rate than the limit derived by Holsapple for his oblate spheroid solutions.

Because this work considers only the surface geometry of the solution shapes, there is no guarantee that the internal stresses of the solution objects are everywhere below the yield stress of the material. However, Holsapple (2001) assumed smooth ellipsoidal objects without surface features, and geometrically an angle of repose-limited object cannot be a smooth ellipsoid because it must have cusps. Because the "surface features" of the objects produced in this work are of a scale comparable to the sizes of the objects themselves, they greatly influence the distribution of gravitational forces within the body, and therefore the ellipsoidal model of the gravitational potential used by Holsapple is not valid for these objects.

Sets of z-axis rotating solutions to the Top configuration, called "Oblate Top" were also found. As seen in Fig. 5, these solutions exhibit some unusual behavior. For the $\phi = 20°$ case, the dependence of α on rotation rate is much stronger than it is for any of the other solutions. For $\phi = 10°$, all of the solutions fall well within the shape limits of Holsapple.

For the Hourglass configuration, the body must be rotated about either its x- or y-axis to achieve stable principal axis rotation for a wide range of rotation rates. It is more difficult to parameterize the Hourglass shape, because it is more like a contact binary than an ellipsoid. In the case of x-axis rotation, which is equivalent to y-axis rotation, it was found that as the rotation rate increased, β remained constant while α decreased. For a range of ϕ values, the ratio $\beta \approx 0.94$. The relationship between rotation rate and α for Hourglass in x-axis rotation is shown in Fig. 5. All Hourglass solutions fall well within Holsapple's shape limits, as shown in Fig. 5. Stable z-axis rotation for Hourglass was observed only for an extremely narrow range of rotation rates near the peak rotation rate, so z-axis rotation for Hourglass is not considered here.

Sandyroid was unable to converge on solutions for either Donut or Top with x- or y-axis rotation. Attempts were also made to produce Jacobi ellipsoids using *Sandyroid* by supplying it with highly elongated initial seed shapes and setting $\phi = 0°$, but these attempts were not successful. The inability of *Sandyroid* to produce Jacobi ellipsoids may indicate that some solutions to Eq. (1) are not numerically stable using the seed growth technique. As Fig. 4 demonstrates, the shapes that *Sandyroid* was capable of producing are objects whose entire surfaces have slopes that are constant within $\pm 1°$.

3. Comparisons between angle of repose-limited bodies and observed small bodies

Unlike fluid bodies, gravitational aggregates can maintain a range of equilibrium shapes. The solution shapes produced

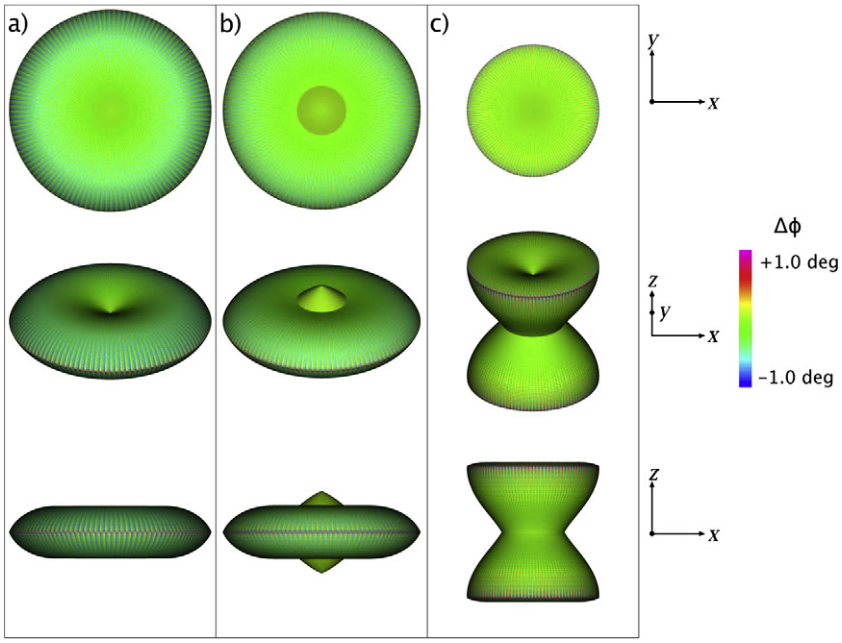

Fig. 4. Highest-angle, non-rotating constant surface angle solutions for (a) Donut ($\phi = 21°$), (b) Top ($\phi = 22°$), and (c) Hourglass ($\phi = 28°$). Three different orientations are shown for each of the three configurations, with the top row corresponding to a view of the top of the objects, the bottom row corresponding to a view of the front of the objects, and the middle row corresponding to an intermediate view. Colors represent the deviation of the surface angle of the facets from the target surface angle, computed using *Polygrav*. Each surface mesh contains 56,400 triangular facets.

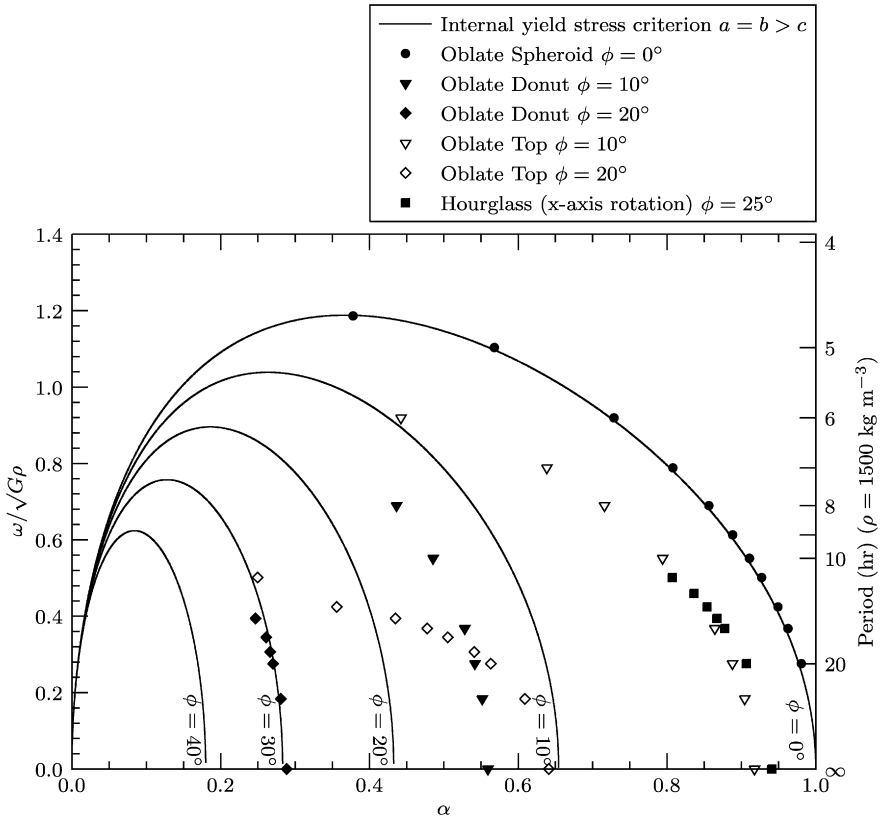

Fig. 5. Relationship between rotation rate and body aspect ratio. The points represent *Sandyroid* solutions for several configurations, angles of repose, and rotation rates. Also plotted are curves of the required angle of internal friction determined by Holsapple (2001) (only the $\sigma_x = \sigma_y < \sigma_z$ branch is shown). The curve for $\phi = 0°$ is the classic Maclaurin spheroid, which is partially reproduced by *Sandyroid*. For each configuration shown here, the most rapidly rotating solution that *Sandyroid* was able to calculate is plotted. Profile generation fails either when a singularity develops in the seed body or the centripetal acceleration becomes greater than the gravitational acceleration at some point along the profile.

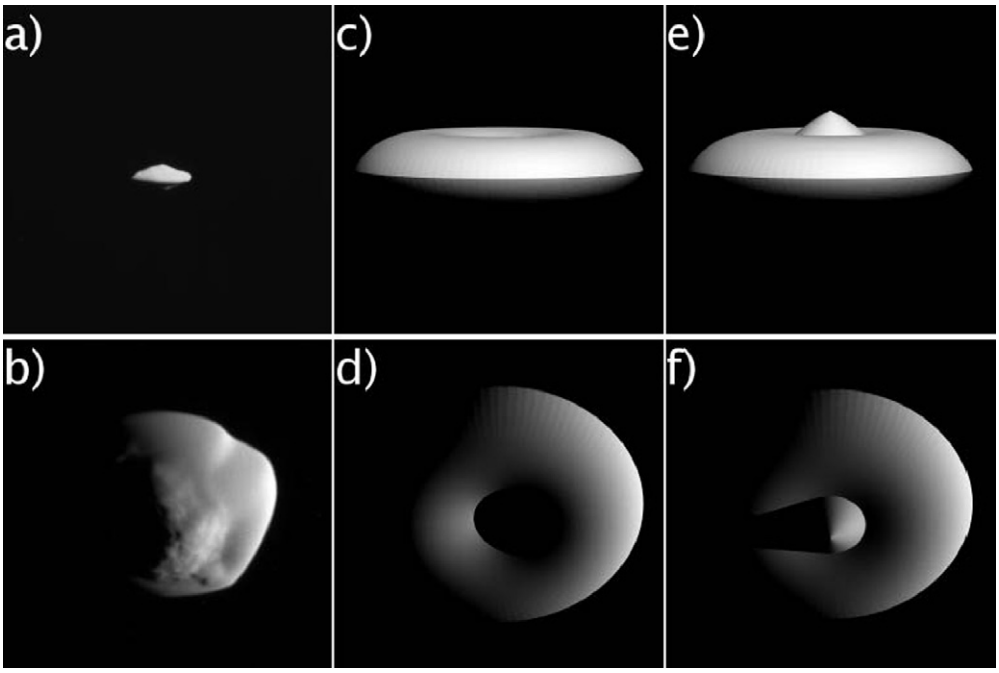

Fig. 6. (a, b) Two views of the saturnian moon Atlas as imaged by the Cassini Imagine Science Subsystem (ISS) narrow angle camera. (c, d) Views of Donut with no rotation and $\phi = 21^\circ$ with similar orientation and lighting as the Atlas images. (e, f) Views of Top with no rotation and $\phi = 22^\circ$ with similar orientation and lighting as the Atlas images. Atlas images courtesy NASA/JPL-Caltech.

by *Sandyroid* represent limiting cases. Because the angle of repose-limited solutions described here are idealized mathematical constructs, some caution is warranted when comparisons are made to the shapes of natural bodies. Nevertheless, some intriguing similarities can be found between the shapes presented here and real small bodies that have been observed.

Radar imaging of the near-Earth Asteroid 1999 KW4 revealed that it has an equatorial ridge that is similar to the positive equatorial cusps found on both Donut and Top (Ostro et al., 2006). The saturnian satellite Atlas shows a striking similarity to both Donut and Top, especially in the equatorial region, as shown in Fig. 6. It has been proposed that the equatorial region of Atlas is composed of ring material that preferentially falls onto the satellite's equator (Brahic et al., 2006; Porco et al., 2006; Thomas et al., 2007). If this is the case, then the shape of Atlas may indicate that the loose ring material may be at or near the angle of repose.

The Hourglass bodies somewhat resemble contact binaries. A comparison of shape models derived from radar of three suspected contact binaries from Neese (2004) to a rotating Hourglass body is shown in Fig. 7. While the Dumbbell seed shape may resemble a contact binary more than the Hourglass solution shapes, it is important to note that *Sandyroid* could not converge on a solution for the Dumbbell configuration over the range of ϕ values explored here. However, due to the inability of *Sandyroid* to find valid solution shapes for a particular configuration even when they are known to exist, it is not known at this time whether a Dumbbell-like configuration admits angle of repose-limited solution shapes or not.

4. Summary

A new technique for calculating self-gravitating constant surface angle objects with rotation called the "seed growth" method has been demonstrated. A numerical code called *Sandyroid* has been developed to implement the seed growth method. *Sandyroid* has produced three classes of constant surface angle shapes, Donut, Top, and Hourglass. The Oblate Donut solutions produced in this work have dimensions that fall outside of the limits derived by Holsapple (2001), except for the $\phi = 0^\circ$ case for which both *Sandyroid* and Holsapple produce solutions consistent with Maclaurin spheroids. Two of the solutions, Donut and Top, have positive cusps along their equator, and similar features are seen in the shapes of real bodies such as 1999 KW4 and Atlas.

The shapes produced by *Sandyroid* are idealized mathematical constructs that represent limiting cases. These shapes are not unique, and as the failure of *Sandyroid* to produce Jacobi ellipsoids demonstrates, there may be other solution shapes that it is incapable of producing. Nevertheless, the shapes that are produced by *Sandyroid* are robust in the sense that the discretized solution objects have surfaces that are computed to be at a constant angle relative to their local gravitational vector, within the limits of mesh resolution.

Acknowledgments

The author thanks James E. Richardson for providing him with the *Polygrav* code and the visualization tool *Gravview*,

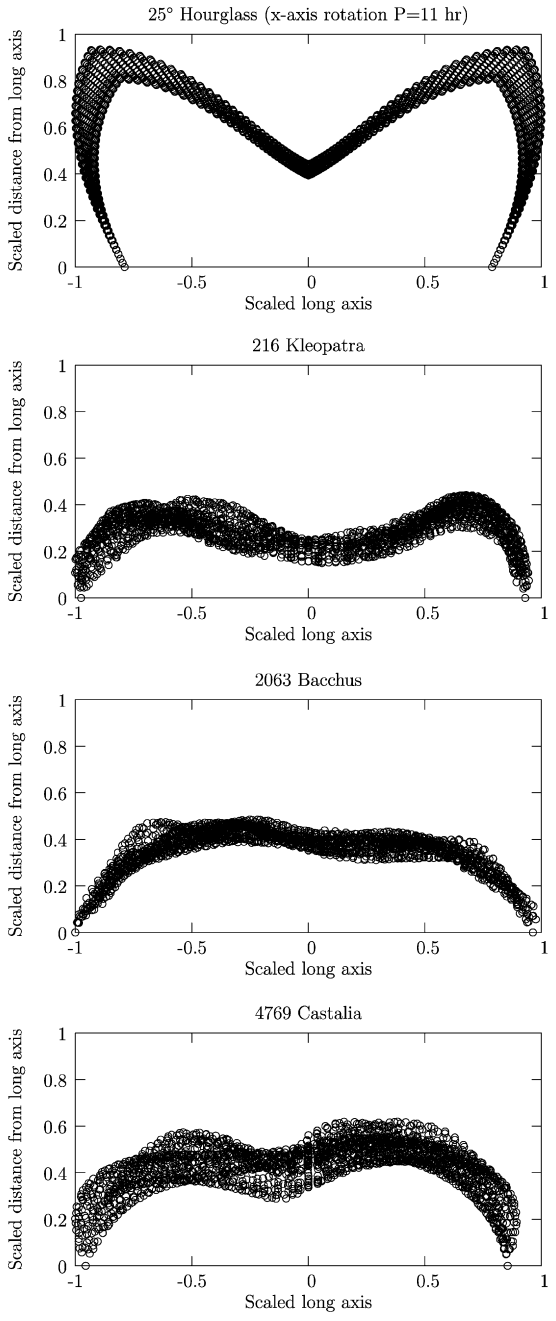

Fig. 7. Rotating Hourglass compared with radar-based shape models of a few proposed contact binary asteroids. Asteroid sizes have been scaled to the largest distance along the longest axis. The origin corresponds to the asteroid center of mass. The shapes produced by *Sandyroid* are idealized models and represent limiting cases. Asteroid shape models are from Neese (2004).

without both of which this project would have been much more difficult. He thanks Derek C. Richardson and Scott Hudson for their thorough and very helpful reviews. He also thanks H. Jay Melosh for providing him with the "seed" for this project, and for his help and encouragement along the way. This research was supported by NASA's Origins of Solar Systems Research Program under Grant No. NNG05GI97G.

References

Brahic, A., Charnoz, S., Déau, E., Thomas, P., Porco, C., 2006. Small satellites embedded in the rings: Accretion and motion of material at the surface of Pan and Atlas. Bull. Am. Astron. Soc. 38, 629. Abstract.

Bretz, M., Cunningham, J.B., Kurczynski, P.L., Nori, F., 1992. Imaging of avalanches in granular materials. Phys. Rev. Lett. 69, 2431–2434.

Buchholtz, V., Pöschel, T., 1994. Numerical investigations of the evolution of sandpiles. Physica A 202, 390–401.

Chandrasekhar, S., 1969. Ellipsoidal Figures of Equilibrium. The Silliman Foundation Lectures. Yale Univ. Press, New Haven.

Holsapple, K.A., 2001. Equilibrium configurations of solid cohesionless bodies. Icarus 154, 432–448.

Holsapple, K.A., 2004. Equilibrium figures of spinning bodies with self-gravity. Icarus 172, 272–303.

Holsapple, K.A., 2007. Spin limits of Solar System bodies: From the small fast-rotators to 2003 EL61. Icarus 187, 500–509.

Holsapple, K.A., Michel, P., 2006. Tidal disruptions: A continuum theory for solid bodies. Icarus 183, 331–348.

Neese, C., 2004. Small body radar shape models V2.0. NASA Planetary Data System, EAR-A-5-DDR-RADARSHAPE-MODELS-V2.0 16.

Ostro, S.J., and 15 colleagues, 2006. Radar imaging of binary near-Earth Asteroid (66391) 1999 KW4. Science 314, 1276–1280.

Porco, C., Weiss, J., Thomas, P., Richardson, D., Spitale, J., 2006. Accretionary origins for Saturn's small satellites: Sizes, shapes, and numerical simulations of growth. Eos (Fall Suppl.) 87, 52.

Richardson, D.C., Leinhardt, Z.M., Melosh, H.J., Bottke Jr., W.F., Asphaug, E., 2002. Gravitational aggregates: Evidence and evolution. In: Bottke Jr., W.F., Cellino, A., Paolicchi, P., Binzel, R.P. (Eds.), Asteroids III. Univ. of Arizona Press, Tucson, pp. 501–515.

Richardson, D.C., Elankumaran, P., Sanderson, R.E., 2005a. Numerical experiments with rubble piles: Equilibrium shapes and spins. Icarus 173, 349–361.

Richardson, J.E., Melosh, H.J., Artemeiva, N.A., Pierazzo, E., 2005b. Impact cratering theory and modeling for the deep impact mission: From mission planning to data analysis. Space Sci. Rev. 117, 241–267.

Thomas, P.C., Burns, J., Charnoz, S., Brahic, A., Porco, C., Weiss, J., 2007. Forming the surfaces of Hyperion, Atlas, and Telesto: Nature versus nurture. Bull. Am. Astron. Soc. 39, 350. Abstract.

Werner, R.A., 1994. The gravitational potential of a homogeneous polyhedron or don't cut corners. Celest. Mech. Dynam. Astron. 59, 253–278.

Withers, P., 2000. Angle of repose-limited shapes of asteroids. Lunar Planet. Sci. XXXI. Abstract 1270.